Quantitative analysis of nanoripple and nanoparticle patterns by grazing incidence small-angle x-ray scattering 3D mapping

D. Babonneau,[*] S. Camelio, E. Vandenhecke, S. Rousselet, M. Garel, and F. Pailloux
Institut Pprime, Département Physique et Mécanique des Matériaux, UPR 3346 CNRS, Université de Poitiers, SP2MI, 11 Boulevard Marie et Pierre Curie, BP 30179, 86962 Futuroscope Chasseneuil Cedex, France

P. Boesecke
ESRF, 6 rue Jules Horowitz, BP 220, 38043 Grenoble Cedex, France
(Received 20 February 2012; published 7 June 2012)

3D reciprocal space mapping in the grazing incidence small-angle x-ray scattering geometry was used to obtain accurate morphological characteristics of nanoripple patterns prepared by broad beam-ion sputtering of Al_2O_3 and Si_3N_4 amorphous thin films as well as 2D arrays of Ag nanoparticles obtained by glancing angle deposition on Al_2O_3 nanorippled buffer layers. Experiments and theoretical simulations based on the distorted-wave Born approximation make it possible to determine the average 3D shape of the ripples and nanoparticles together with crucial information on their in-plane organization. In the case of nanoparticle arrays, the approach was also used to quantify the growth conformity of an additional capping layer, which proceeds by replication of the buried ripple pattern.

DOI: 10.1103/PhysRevB.85.235415 PACS number(s): 61.05.cf, 61.46.−w, 81.07.−b, 81.16.Rf

I. INTRODUCTION

Uniform ion-beam sputtering (IBS) at low energy (∼keV) has emerged in recent decades as a promising bottom-up approach to produce a remarkable variety of regular nanoscale patterns on solid surfaces, such as self-organized nanodots, nanoholes, and nanoripples, with periodicities varying from a few nm to several μm.[1–4] The major advantages of such a simple and low-cost method compared with top-down lithography or other self-assembling techniques rely on its capability to pattern large surface areas up to several cm^2 in a one-step process and a short time. Moreover, IBS has proved its applicability to a wide range of crystalline or amorphous materials, including metals,[5] semiconductors,[6] insulators,[7] and polymers.[8]

While nanodots and nanoholes can be produced at normal ion incidence, IBS under off-normal incidence usually results in the generation of unidimensional ripples. According to the classical theory of Bradley and Harper,[9] the formation of periodic nanoripple patterns on amorphous or amorphizable surfaces arises from an instability caused by the interplay between a surface curvature dependence of the sputtering yield (that induces roughening) and smoothing by different surface relaxation mechanisms. More recently, the linear Bradley-Harper's theory has been generalized to include nonlinear and noise terms,[4,10–13] which can modify the long term behavior of the surface evolution (e.g., amplitude saturation, order enhancement, wavelength coarsening, etc.). Also, the nonlinear nature of the pattern formation process as well as shadowing effects, may result in a change of the ripple profile from a sinusoidal to an asymmetric sawtooth morphology.[14,15]

The different continuum models proposed so far to explain ripple formation by IBS are based on the Sigmund's cascade collision theory[16] to describe the sputtering (roughening) phenomena and, more specifically, to estimate the energy deposited in the near-surface region by an impinging ion. Regarding the competing smoothing process, various relaxation mechanisms have been proposed, which can be thermally activated or ion induced.[11] For instance, in the particular case of ripples created by IBS on insulating surfaces at room temperature, it is commonly accepted that the surface smoothing is dominated by surface-confined ion-enhanced viscous flow.[14,17,18] Within this context, IBS offers a strong flexibility to tune the morphology and the periodicity of regular arrays of unidimensional ripples by changing the process parameters (e.g., target temperature, ion mass, energy and incidence angle, ion flux, and total fluence) or the nature of the target material (atomic mass, binding energies, density, surface tension, and surface viscosity).[1]

Because the topography of the substrate can affect significantly the growth of deposited thin films, anisotropic nanoripple patterns induced by IBS have recently become popular to be used as templates for further processing.[8,19–24] For example, it has been shown that the conformal growth of magnetic thin films on rippled surfaces may result in substantial modifications of in-plane uniaxial anisotropy.[25–31] Moreover, nanorippled surfaces have received special attention lately to fabricate self-aligned noble metal nanoparticles or nanowires with anisotropic plasmonic properties,[32–36] which can be tuned by varying the ripple wavelength, the substrate temperature, the angle of incidence and the direction of metal atoms with respect to the ripples, the deposition rate and time, etc. However, from a technological point of view, the scalable templated growth of self-organized metal nanoparticles and nanowires with tailored magnetic or optical anisotropies requires a precise control of the prepatterned surface morphology as well as of the size, shape, and spatial organization of the metal nanostructures. Structural characterizations of nanoripple and nanoparticle patterns prepared by IBS with subsequent thin film growth are generally limited to direct imaging techniques, such as atomic force microscopy (AFM), scanning electron microscopy, or transmission electron microscopy. While these "local" techniques probe a small sample area of the order of 1 μm^2 or even less, x-ray scattering methods are able to

 ©2012 American Physical Society

provide information averaged over macroscopic dimensions. In this respect, grazing incidence small-angle x-ray scattering (GISAXS) has recently emerged as an ideal complementary tool to observe *ex situ* or *in situ* surface modifications induced by IBS (including metallic,[37–40] semiconducting,[41–48] and insulating[14,17] surfaces) and growth of nanostructures[24,35,36] or thin films[19,22] on such prepatterned surfaces. Nevertheless, because GISAXS is a "nonlocal" technique that probes nanostructures by exploring the reciprocal space,[49] careful data analysis is often required to get full quantitative information in real space.

Here, we present detailed studies of quantitative GISAXS measurements of nanoripple patterns produced by IBS on Al_2O_3 and Si_3N_4 amorphous thin films as well as Ag nanoparticle arrays obtained by IBS deposition at glancing incidence on Al_2O_3 nanorippled templates. Despite the intrinsic in-plane anisotropy of unidimensional nanoripple patterns, the majority of previous GISAXS experiments reported so far have been done with the incident x-ray beam parallel to the ripples using linear[14,17,43,47,48] or 2D detectors.[22,24,35,36] However, while in the case of isotropic patterns one 2D GISAXS measurement at a generic azimuth φ is enough to gather information about the morphological parameters of the whole array, the 2D GISAXS signal must be recorded at different φ to obtain a full 3D intensity map in the case of anisotropic patterns.[6] In this article, we show that 3D GISAXS mapping associated with further modeling effort to analyze quantitatively the distribution of scattered intensity in the reciprocal space is a convenient approach to characterize nanoripple and nanoparticle patterns with high sensitivity and excellent statistical accuracy. The article is organized as follows: Section II is dedicated to the description of the GISAXS theory, simulations and experiments of nanoripple patterns on amorphous surfaces whereas Sec. III focuses on the GISAXS analysis of anisotropic 2D arrays of Ag nanoparticles sandwiched between amorphous Al_2O_3 layers; finally, a summary of the results is presented in Sec. IV.

II. GISAXS FROM RIPPLED THIN FILMS

A. Analytical model

The scattering geometry for performing 3D GISAXS reciprocal space mapping is shown in Fig. 1, where the incident x-ray beam impinges on the surface at an angle α_i and the scattered intensity is measured as a function of the in-plane and out-of-plane exit angles $(2\theta_f,\alpha_f)$. The corresponding components of the momentum transfer $\vec{q} = (q_x,q_y,q_z)$ are given by

$$\vec{q} = \frac{2\pi}{\lambda}\mathcal{R}_z \begin{pmatrix} \cos(2\theta_f)\cos(\alpha_f) - \cos(\alpha_i) \\ \sin(2\theta_f)\cos(\alpha_f) \\ \sin(\alpha_f) + \sin(\alpha_i) \end{pmatrix}, \tag{1}$$

where λ is the x-ray wavelength and $\mathcal{R}_z$ is the rotation matrix about the normal to the sample surface,

$$\mathcal{R}_z = \begin{pmatrix} \cos(\varphi) & \sin(\varphi) & 0 \\ -\sin(\varphi) & \cos(\varphi) & 0 \\ 0 & 0 & 1 \end{pmatrix}, \tag{2}$$

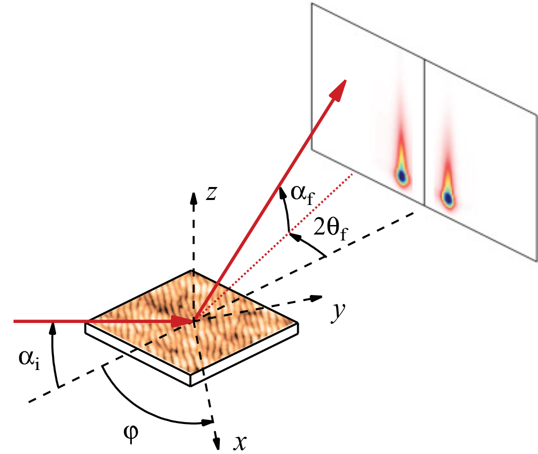

FIG. 1. (Color online) Schematic drawing of the scattering geometry used to perform 3D GISAXS reciprocal space mapping. α_i denotes the angle of incidence, φ is the in-plane rotation angle, and $(2\theta_f,\alpha_f)$ are the in-plane and out-of-plane angles of emergence. The z direction is normal to the sample surface, while the x and y directions are in the surface plane.

with φ being the in-plane rotation (azimuth) angle used to align the nanostructures with respect to the incoming beam (the z direction is taken along the sample normal, while the x direction and the projected direction of the incident x-ray beam onto the sample plane are antiparallel at $\varphi = 0^\circ$).

For polydispersed systems, the GISAXS intensity is commonly calculated within the local monodisperse approximation, which considers locally monodisperse domains that interfere incoherently,[50]

$$\mathcal{I}(\vec{q}) \propto \int_0^\infty |\mathcal{F}(\vec{q})|^2 \mathcal{S}(\vec{q}) \mathcal{N}(W)\, dW, \tag{3}$$

where $\mathcal{F}(\vec{q})$ is the form factor of the scattering objects, $\mathcal{S}(\vec{q})$ is the structure factor due to the spatial correlation, and $\mathcal{N}(W)$ is the size distribution function. Moreover, at grazing incidence conditions, dynamical scattering effects have to be taken into account since the Born approximation (BA) fails in reproducing the measured data so long as $\alpha_{i,f}$ are close to the critical angle of total reflection. In the framework of the distorted-wave Born approximation (DWBA), the form factor of nanostructures supported on a stratified medium is then given by[51]

$$\begin{aligned} \mathcal{F}(q_\parallel,q_z) = {} & F\left(q_\parallel,k_z^f - k_z^i\right) + R_0^+(\alpha_i)\, F\left(q_\parallel,k_z^f + k_z^i\right) \\ & + R_0^+(\alpha_f)\, F\left(q_\parallel,-k_z^f - k_z^i\right) \\ & + R_0^+(\alpha_i)\, R_0^+(\alpha_f)\, F\left(q_\parallel,-k_z^f + k_z^i\right), \end{aligned} \tag{4}$$

where $q_\parallel = \sqrt{q_x^2 + q_y^2}$ and $q_z = k_z^f - k_z^i$ are the in-plane and out-of-plane components of the momentum transfer, R_0^+ is the reflectivity of the underlying stacking, which can be calculated by applying the Abélès matrix formalism,[52,53] and $F(q_\parallel,k_z^i,k_z^f)$ is the form factor of the scattering objects calculated in the BA (i.e., the Fourier transform of their shape).

Afterward, an asymmetric sawtooth profile with a positive slope γ_+ and a negative slope γ_- has been used as a simplified approximation to the ripple shape, as depicted in Fig. 2. It

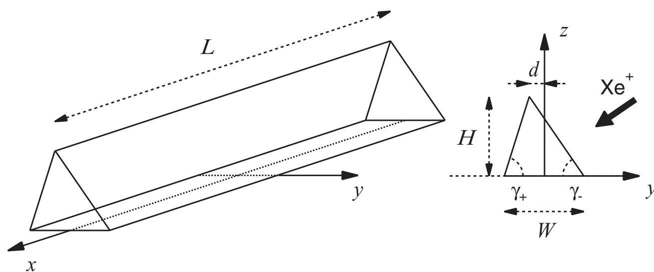

FIG. 2. Representation of the shape used to model the form factor of the ripples. The direction of the Xe^+ ion beam is also indicated.

should be noted that depending on the experimental conditions (type of ion and material, ion energy, and incidence angle, etc.), γ_+ can be either higher or smaller than γ_-, i.e., the long side of the ripples can be either pointing toward the ion beam[14] or be opposite,[15] respectively. Assuming straight ripples oriented along the x direction, the form factor in the BA can be expressed as

$$F(\vec{q}) = L\,\mathrm{sin_c}\left(q_x \frac{L}{2}\right) W \times \int_0^H \left(1 - \frac{z}{H}\right) \mathrm{sin_c}\left[q_y \frac{W}{2}\left(1 - \frac{z}{H}\right)\right] \times \exp\left\{-i\left[q_y A \frac{W}{2}\left(1 - \frac{z}{H}\right) + q_z z\right]\right\} dz, \quad (5)$$

where W is the ripple width, L is the ripple length, H is the ripple height, and $A = 2d/W$ is the asymmetry factor of the ripples ($-1 \leqslant A \leqslant 1$) with $\tan\gamma_\pm = 2H/[W(1 \mp A)]$. It is worth noting that a symmetric profile ($A = 0$) yields $\tan\gamma_+ = \tan\gamma_- = 2H/W$, while a positive asymmetry factor ($A > 0$) corresponds to a ripple profile with $\gamma_+ > \gamma_-$. Besides, the structure factor has been calculated within the 1D-paracrystal theory,[54] with the scatterers being considered as isolated objects along the x direction and the surface supposed to be fully covered by ripples (i.e., their lateral period and width are equal),

$$\mathcal{S}(\vec{q}) = \frac{1 - \phi^2}{1 - 2\phi\cos(q_y W) + \phi^2}, \quad (6)$$

where $\phi = \exp[-q_y^2 W^3/(4\xi_y)]$ and ξ_y is the lateral correlation length of the ordered domains in a short-range order scenario.[6] In this model, ξ_y can be interpreted as a measure of local uniformity of the ripple pattern whereas $\mathcal{N}(W)$ [see Eq. (3)] represents the size distribution at a macroscopic level, which is supposed to follow a log-normal function specified by its full width at half maximum (FWHM) σ_W.

B. GISAXS simulations

GISAXS calculations were performed using Eqs. (3)–(6) for nanoripple patterns formed at the surface of a 20-nm-thick Al_2O_3 film deposited on a Si substrate. The x-ray wavelength was fixed at $\lambda = 0.16$ nm, the angle of incidence was $\alpha_i = 0.3°$, and the densities of the film and the substrate were 3.25 and 2.33 g cm^{-3}, respectively. Figure 3(a) shows the 2D GISAXS pattern ($2\theta_f$,α_f) calculated at $\varphi = 0°$ for

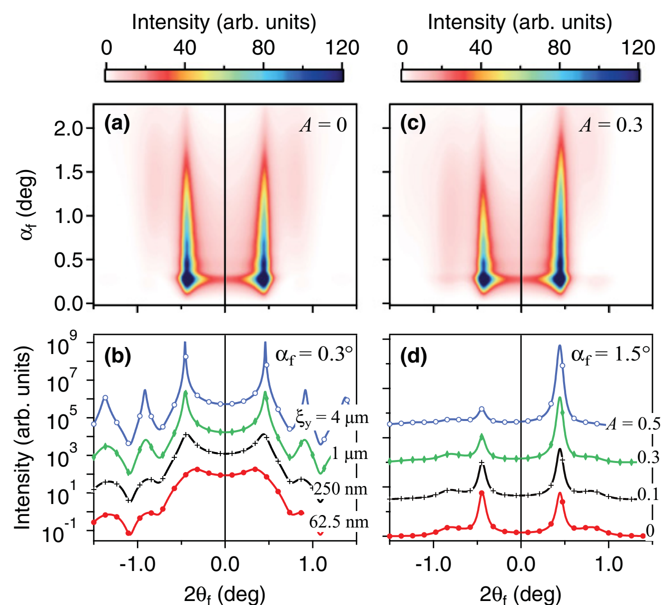

FIG. 3. (Color online) GISAXS intensity calculated at $\varphi = 0°$ for periodic nanoripples with $W = 20$ nm, $H = 4$ nm, $L = 100$ nm, and $\sigma_W = 0$. (a) Out-of-plane ($2\theta_f$,α_f) map with $A = 0$ and $\xi_y = 250$ nm. (b) Line profiles (logarithmic scale) drawn at $\alpha_f = 0.3°$ for different ξ_y values ($A = 0$). (c) Out-of-plane ($2\theta_f$,α_f) map with $A = 0.3$ and $\xi_y = 250$ nm. (d) Line profiles (linear scale) drawn at $\alpha_f = 1.5°$ for different A values ($\xi_y = 250$ nm). Curves in (b) and (d) are shifted upward for clarity.

symmetric nanoripples ($A = 0$) with $W = 20$ nm, $H = 4$ nm, $L = 100$ nm, $\xi_y = 250$ nm, and $\sigma_W = 0$. As a result of the lateral correlation between ripples, two vertical streaks (whose perpendicular extension is inversely proportional to the ripple height) are exhibited at $2\theta_{f,max} \approx \pm 0.44°$. The influence of the lateral correlation length ξ_y can be probed by plotting line profiles for a given α_f value. As seen in Fig. 3(b), a decrease of ξ_y leads to a streak shift toward smaller $2\theta_{f,max}$ values together with a broadening and damping of the first, second, and third order satellite peaks. Furthermore, while the GISAXS signal is symmetric in the horizontal direction when $A = 0$, the 2D GISAXS pattern calculated with $A = 0.3$ clearly presents an asymmetry in the intensity distribution [Fig. 3(c)], which can be ascribed to the asymmetric profile of the rippled surface.[14,17,47] Line profiles drawn at $\alpha_f = 1.5°$ also show that such an effect is all the more pronounced as A is larger [Fig. 3(d)], but has a negligible influence on the streak position along $2\theta_f$.

In-plane GISAXS maps ($2\theta_f$,φ) calculated at $\alpha_f = 0.3°$ and $\alpha_f = 1.5°$ with $A = 0.3$ are presented in Figs. 4(a) and 4(b), respectively. Both maps show elongated spots located at $\pm 2\theta_{f,max}$ whose vertical extension $\Delta\varphi$ (FWHM) is inversely proportional to the ripple length L. Furthermore, the asymmetric shape of the ripples is confirmed by an asymmetry in the in-plane intensity distribution. However, while this asymmetry remains weak for $\alpha_f = 0.3°$ with two spots of similar intensities (intensity ratio $\sim$1.1) centered at $\varphi = 0°$, the characteristics of the spots observed for $\alpha_f = 1.5°$ are obviously very different both in intensity (intensity ratio $\sim$2.5) and position with the spot at $\pm 2\theta_{f,max}$ peaking at $\varphi \approx \pm 3°$. The

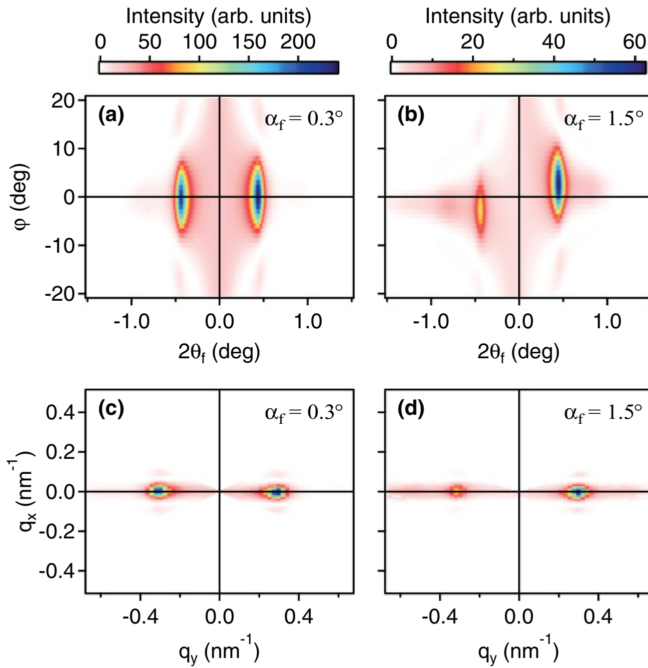

FIG. 4. (Color online) In-plane GISAXS maps $(2\theta_f,\varphi)$ calculated at (a) $\alpha_f = 0.3^\circ$ and (b) $\alpha_f = 1.5^\circ$ for periodic nanoripples with $W = 20$ nm, $H = 4$ nm, $L = 100$ nm, $\xi_y = 250$ nm, $\sigma_W = 0$, and $A = 0.3$. (c) and (d) Corresponding GISAXS maps (q_y,q_x).

corresponding GISAXS maps plotted as a (q_y,q_x) picture in Figs. 4(c) and 4(d) exhibit the spots at $q_y \approx \pm 0.3$ nm^{-1} and $q_x = 0$ for both $\alpha_f = 0.3^\circ$ and $\alpha_f = 1.5^\circ$, while the intensity ratio depends indeed on α_f.

The influence of the ripple asymmetry on the 3D GISAXS intensity can be investigated in more detail by defining an asymmetry ratio $AR(\varphi,\alpha_f)$ as

$$AR = \frac{\mathcal{I}(+2\theta_{f,\max}) - \mathcal{I}(-2\theta_{f,\max})}{\mathcal{I}(+2\theta_{f,\max}) + \mathcal{I}(-2\theta_{f,\max})}, \quad (7)$$

where $\mathcal{I}(\pm 2\theta_{f,\max})$ is the intensity measured at $2\theta_f = \pm 2\theta_{f,\max}$ for a given (φ,α_f) position. As seen in Figs. 5(a) and 5(b), $AR(\varphi,\alpha_f)$ maps calculated with $A = 0$ and $A = 0.3$ confirm that the absolute value of the asymmetry ratio tends to decrease to 0 over a wide φ range for $\alpha_f < \alpha_i$. Moreover, isointensity lines for $A = 0$ show that $AR(\varphi,\alpha_f) = 0$ at $\varphi = 0^\circ$ only [Fig. 5(a)]. Accordingly, asymmetric GISAXS patterns are obtained even from a symmetric profile whenever the incident x-ray beam is not parallel to the ripples, with $AR(\varphi,\alpha_f)$ having the same sign as φ. In contrast, for $A = 0.3$ [Fig. 5(b)], the isointensity line corresponding to $AR(\varphi,\alpha_f) = 0$ does not draw a straight vertical line neither at $\varphi = 0^\circ$ nor at any other φ position. This behavior indicates that it is not possible to obtain a symmetric GISAXS pattern from asymmetric ripples, even after misorientation of the sample with respect to the incident x-ray beam. Accordingly, it appears that azimuthal scans are required to detect unambiguously an asymmetric ripple profile. Moreover, a precise determination of the zero azimuth is mandatory to retrieve quantitative information on the ripple morphology (i.e., width, height, length, and asymmetry).

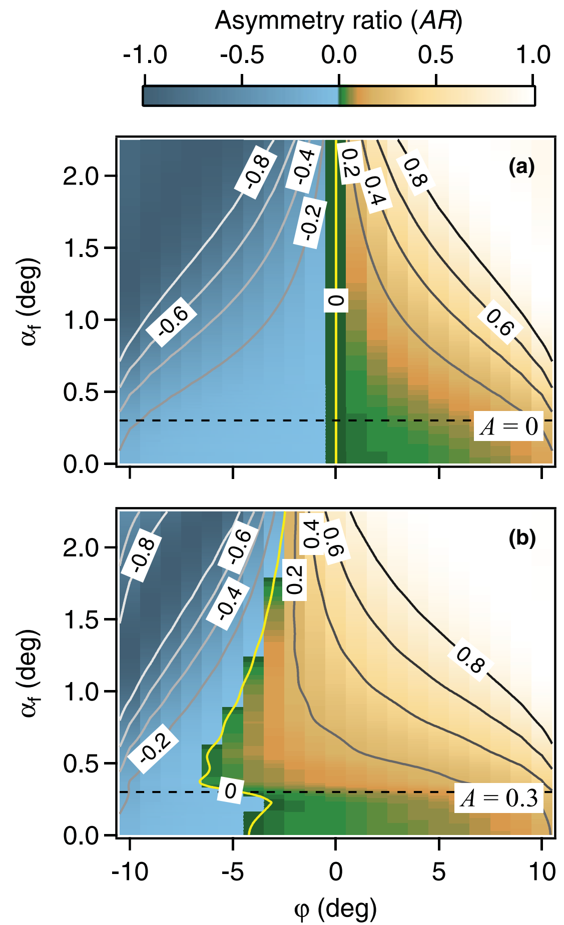

FIG. 5. (Color online) Asymmetry ratio $AR(\varphi,\alpha_f)$ calculated with (a) $A = 0$ and (b) $A = 0.3$ ($W = 20$ nm, $H = 4$ nm, $L = 100$ nm, $\xi_y = 250$ nm, and $\sigma_W = 0$). The dotted lines represent the position $\alpha_f = \alpha_i = 0.3^\circ$.

C. Results

1. Experimental details

Nanoripple patterns were produced on dielectric surfaces by a procedure described elsewhere,[35] which consists in combining thin film deposition with subsequent patterning by defocused ion erosion in a dual ion-beam sputtering Nordiko™ chamber. Deposition of amorphous Al_2O_3 and Si_3N_4 thin films onto silicon substrates was accomplished with a base pressure of about 4×10^{-8} Torr at a rate of 0.15 nm s^{-1} for Al_2O_3 and 0.07 nm s^{-1} for Si_3N_4, respectively. Ion erosion of the as-grown films was carried out with Xe^+ ions at a sputtering angle of $\vartheta = 55^\circ$ with respect to the surface normal, with an ion energy $E = 1$ keV, and a fluence of about 2.5×10^{16} ions cm^{-2} (ion flux $\sim 1.4 \times 10^{14}$ ions cm^{-2} s^{-1}), leading to ripples that are oriented perpendicular to the ion beam.[35] During thin film deposition and ion erosion, the temperature was maintained around 20 °C for Al_2O_3 and 200 °C for Si_3N_4, respectively. As-etched thin films were characterized by x-ray reflectivity and spectroscopic ellipsometry measurements to determine their density, thickness, and the erosion rate as reported in Table I.

GISAXS measurements were performed at the ID01 beamline at the ESRF (Grenoble, France) using a Princeton

TABLE I. Parameters retrieved from x-ray reflectivity and GISAXS analyses of as-etched Al_2O_3 and Si_3N_4 thin films. Assuming the ripple width to be log normally distributed at a macroscopic level, ln W is the mean of the ripple width logarithm, σ_W is the full width at half maximum of the distribution, while L is the ripple length, H is the ripple height, ξ_y is the lateral correlation length, and A is the asymmetry factor of the ripples.

Material	Density (g/cm^3)	Thickness (nm)	Erosion rate (nm/s)	W (nm)	σ_W (nm)	L (nm)	H (nm)	ξ_y (nm)	A
Al_2O_3	3.25	20.8	0.25	20.5	5.0	80.1	4.7	641	0.137
Si_3N_4	3.44	52.0	0.49	20.5	4.5	54.7	3.5	283	0.138

Instruments charge-coupled device area detector placed in vacuum inside a flight tube at 1200 mm from the sample. The energy of the x-ray beam was set to 7.75 keV ($\lambda = 0.16$ nm) and the angle of incidence was chosen to be close to the critical angle for total external reflection of the dielectric films (i.e., $\alpha_c = 0.271^\circ$ and $\alpha_c = 0.281^\circ$ for Al_2O_3 and Si_3N_4, respectively) to enhance the surface sensitivity. 3D GISAXS reciprocal space mapping of the nanoripple patterns was performed by collecting series of 2D GISAXS patterns ($2\theta_f,\alpha_f$) for different azimuth angles starting from $\varphi = 0^\circ$ to $\varphi = 90^\circ$ by increments of 1°, with the projected direction of the Xe^+ ion beam onto the sample plane being opposite to the y direction as seen in Fig. 2 (i.e., the projected directions of the Xe^+ ion beam and of the incident x-ray beam are antiparallel at $\varphi = 90^\circ$). According to the simulations presented in Sec. II B, the exact position of the zero azimuth was determined experimentally by performing preliminary scans in order to identify the intensity maximum at $\alpha_f = \alpha_i$ and $2\theta_f = \pm 2\theta_{f,max}$. The experimental data were analyzed with the FITGISAXS package[55] developed within the IGOR Pro software (WaveMetrics, Inc.).

2. GISAXS analysis

Figures 6(a) and 7(a) show the experimental 2D GISAXS patterns ($2\theta_f,\alpha_f$) taken at $\varphi = 0^\circ$ for the as-etched Al_2O_3 and Si_3N_4 thin films, respectively, which exhibit a set of asymmetric streaks with the intensity of the streak located on the positive $2\theta_f$ side being noticeably higher than the one on the negative $2\theta_f$ side (i.e., $AR > 0$). The corresponding experimental in-plane GISAXS maps ($2\theta_f,\varphi$) obtained at $\alpha_f = 0.425^\circ$ are displayed in Figs. 6(b) and 7(b), which show elongated spots centered at $\varphi \approx 0^\circ$ with angular distribution $\Delta\varphi = 12^\circ$ and $\Delta\varphi = 18^\circ$, respectively. These results indicate unambiguously that both the Al_2O_3 and Si_3N_4 surfaces present a uniform ordered pattern of unidirectional and asymmetric ripples with $\gamma_+ > \gamma_-$ (as depicted in Fig. 2), in agreement with previous observations made on ion-eroded Si, SiO_2, and sapphire surfaces.[14,17,22,47,56] However, qualitatively, the ripples formed on Al_2O_3 are longer than the ripples formed on Si_3N_4. It should be noted that the increase of $\Delta\varphi$ may also be an indication of the formation of ripples not perfectly straight or aligned.

The full in-plane and out-of-plane GISAXS maps were fitted using a Levenberg-Marquardt χ^2 criterion minimization[57] by using W, σ_W, L, H, ξ_y, and A as quantitative parameters. The best-fit parameters are gathered in Table I and the corresponding simulated maps are displayed in Figs. 6(c) and 6(d) and Figs. 7(c) and 7(d). It is worth noting that the experimental data are well reproduced with $W = 20.5$ nm and $A = 0.14$ for both the Al_2O_3 and Si_3N_4 thin films. However, obvious discrepancies can be pointed out regarding other parameters such as H, L, and ξ_y, which confirms that the morphology of the ripples depends on the nature of the etched material. In particular, it appears that both the lateral correlation length ξ_y and the ripple length L are smaller for the ion-etched Si_3N_4 surface than the ion-etched Al_2O_3 surface. These results reflect the achievement of a higher degree of ordering on the rippled Al_2O_3 surface, which can be ascribed to intrinsic properties of the amorphous Al_2O_3 and Si_3N_4 materials having different physical parameters (e.g., sputtering parameters through the Sigmund's theory, surface tension, surface viscosity, etc.). Nevertheless, the influence of other extrinsic effects such as different erosion temperature and rate (20 °C and 0.25 nm s^{-1} for Al_2O_3 compared to 200 °C and 0.49 nm s^{-1} for Si_3N_4) cannot be ruled out. For example, it has been reported that nanodot patterns produced by IBS of Si(001) become less ordered above 150 °C.[44] Moreover, order enhancement of self-organized nanodots on Si (Ref. 45) and GaSb (Ref. 46) surfaces has been observed at lower rate.

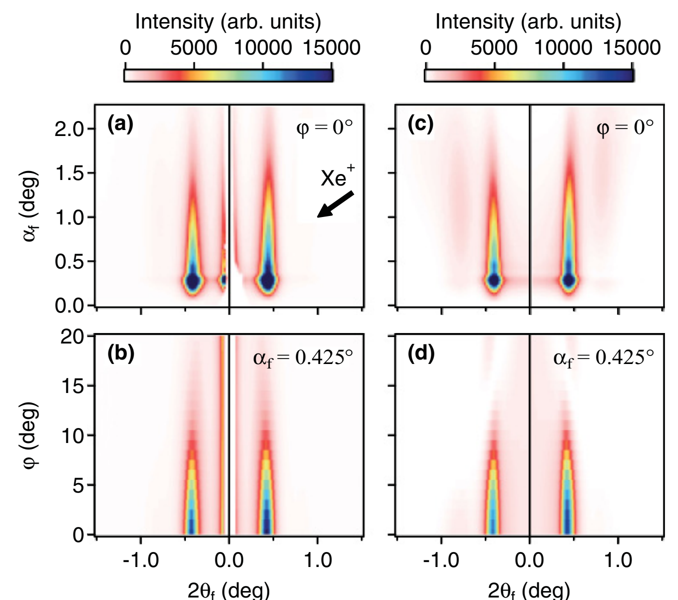

FIG. 6. (Color online) GISAXS analysis of the as-etched Al_2O_3 thin film. (a) Experimental out-of-plane ($2\theta_f,\alpha_f$) map at $\varphi = 0^\circ$. (b) In-plane ($2\theta_f,\varphi$) map at $\alpha_f = 0.425^\circ$. (c) Simulated out-of-plane map. (d) Simulated in-plane map. The direction of the Xe^+ ion beam is indicated by the arrow in (a).

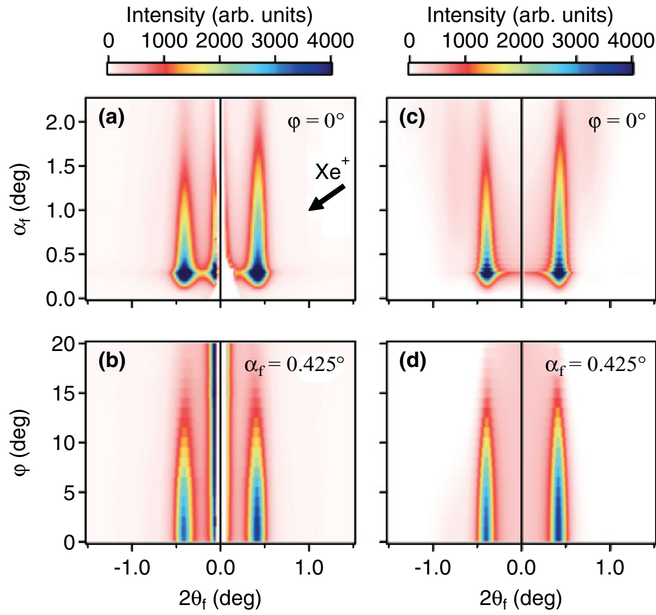

FIG. 7. (Color online) GISAXS analysis of the as-etched Si_3N_4 thin film. (a) Experimental out-of-plane $(2\theta_f,\alpha_f)$ map at $\varphi = 0°$. (b) In-plane $(2\theta_f,\varphi)$ map at $\alpha_f = 0.425°$. (c) Simulated out-of-plane map. (d) Simulated in-plane map. The direction of the Xe^+ ion beam is indicated by the arrow in (a).

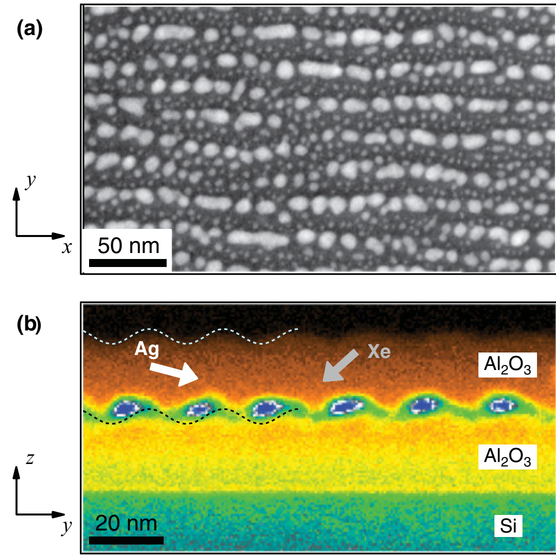

FIG. 8. (Color online) HAADF-STEM images of Al_2O_3-capped Ag nanoparticles grown on rippled Al_2O_3 thin films. (a) Plan view, Ag amount of 2.8 nm, and (b) cross-section view, Ag amount of 1.4 nm. The dark and bright dotted lines are guides to the eye, which mark the buffer/capping and capping/air interfaces, respectively.

III. GISAXS FROM ORDERED NANOPARTICLES IN THIN FILMS

A. Sample preparation and "local" characterizations

Al_2O_3 rippled thin films were used as templates with the aim of creating self-organized Ag nanoparticle patterns using the procedure described in Refs. 35 and 36. Deposition of Ag amounts of 1.4 and 2.8 nm, respectively, was accomplished at a temperature of 20 °C and a rate of 0.07 nm s^{-1} by IBS under a glancing incidence of 5° from the surface, with the atomic flux being oriented opposite to the Xe^+ beam. Subsequently, the Ag nanoparticles were covered with an additional 20-nm-thick amorphous Al_2O_3 capping layer deposited at normal incidence to preserve silver from the external environment. The samples were examined by GISAXS at the ID01 beamline using the same geometry as described in Sec. II C1. The Ag nanoparticle patterns were also characterized by high-angle annular dark-field scanning transmission electronic microscopy (HAADF-STEM) with a JEOL 2200FS microscope using an acceleration voltage of 200 kV, a probe size of 0.7 nm, and an inner collection angle of 50 mrad.

As a typical example, Fig. 8(a) shows a plan-view HAADF-STEM image of the Ag nanoparticles sandwiched between Al_2O_3 layers resulting from the deposition of an Ag amount of 2.8 nm. Glancing angle deposition associated with Volmer-Weber growth on the rippled Al_2O_3 surface results in the formation of bimodal size-distributed nanoparticles with small particles (diameter<4 nm) intercalated among lines of larger particles. The latter are predominantly aligned and elongated along the x direction perpendicular to the Ag atomic flux (i.e., along the ripples) with an average in-plane aspect ratio that can be estimated as $D_x/D_y \approx 1.2$ and an average interparticle distance along the y direction $\Lambda_y \approx 20$ nm close to the ripple width W (Table I). Furthermore, while a replication of the lateral order between ripples is achieved in the y direction, a larger disorder appears in the x direction. A representative cross-sectional HAADF-STEM image of the nanoparticle pattern resulting from the deposition of an Ag amount of 1.4 nm is also displayed in Fig. 8(b). Because part of the Ag atomic flux is shadowed by the surface topography during the glancing angle deposition, preferential Ag growth occurs on the illuminated slopes of the rippled surface,[32,35] thus leading to large nanoparticles tilted from the surface normal by a tilt angle of γ_+. Furthermore, it can be observed that the surface roughness of the Al_2O_3 capping layer tends to replicate the topography of the underlying rippled interface.

B. GISAXS modeling and simulations

In the case of a 2D rectangular lattice of nanoparticles buried in a flat thin film at a depth z, the structure factor can be calculated within the paracrystal theory as follows:

$$\mathcal{S}(\vec{q}) = \prod_{j=x,y} \frac{1-\phi_j^2}{1-2\phi_j\cos(q_j\Lambda_j)+\phi_j^2}, \tag{8}$$

where $\phi_j = \exp[-q_\parallel^2\Lambda_j^3/(4\xi_j)]$, Λ_j and ξ_j are the interparticle distance and correlation length along the direction j, respectively. Moreover, neglecting correlated roughness effects, the form factor in the DWBA can be expressed as

$$\begin{aligned}\mathcal{F}(q_\parallel,q_z) = {} & A_z^-(\alpha_i)\,A_z^-(\alpha_f)\,F\left(q_\parallel,\widetilde{k}_z^f-\widetilde{k}_z^i\right)\\ & +A_z^+(\alpha_i)\,A_z^-(\alpha_f)\,F\left(q_\parallel,\widetilde{k}_z^f+\widetilde{k}_z^i\right)\\ & +A_z^-(\alpha_i)\,A_z^+(\alpha_f)\,F\left(q_\parallel,-\widetilde{k}_z^f-\widetilde{k}_z^i\right)\\ & +A_z^+(\alpha_i)\,A_z^+(\alpha_f)\,F\left(q_\parallel,-\widetilde{k}_z^f+\widetilde{k}_z^i\right),\end{aligned} \tag{9}$$

where $\widetilde{k}_z^{i,f}$ are the z components of the wave vectors in the film considering the refraction effect at the film surface, and

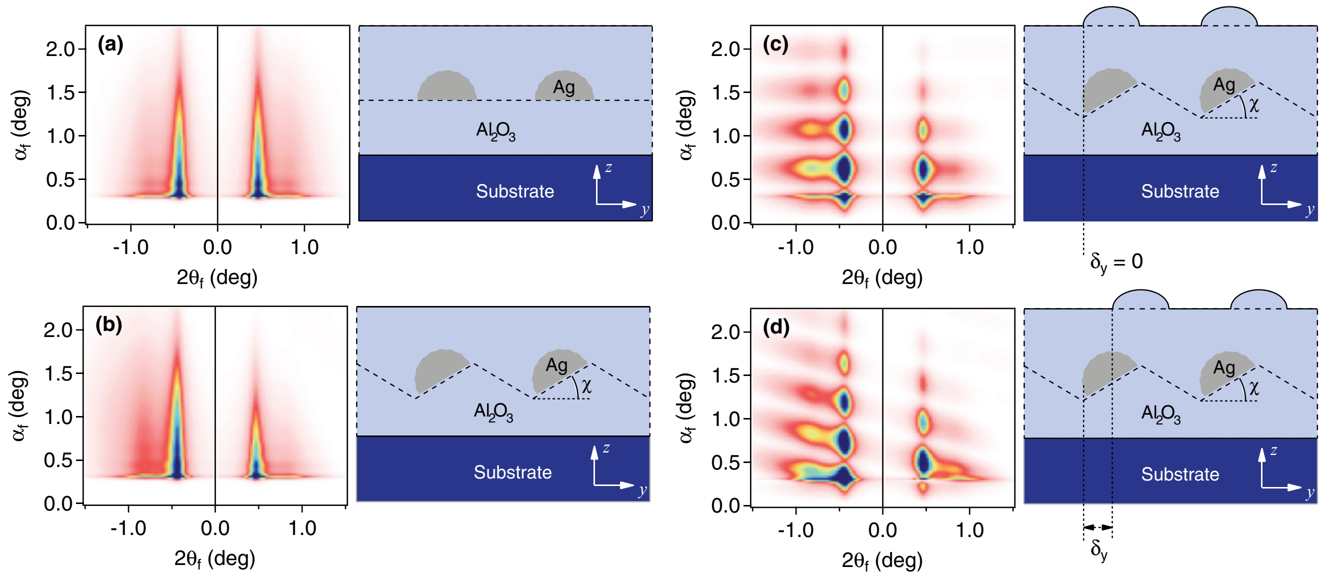

FIG. 9. (Color online) GISAXS intensity calculated at $\varphi = 0°$ for Al_2O_3-capped Ag nanoparticles grown on rippled Al_2O_3 thin films (linear color scale). (a) $\chi = 0°$, no correlated roughness. (b) $\chi = 21.8°$, no correlated roughness. (c) $\chi = 21.8°$, correlated roughness with $\delta_y = 0$. (d) $\chi = 21.8°$, correlated roughness with $\delta_y = \Lambda_y/4$. The corresponding configurations are also sketched in cross-section view.

A_z^+ and A_z^- are the complex amplitudes of the upward and downward propagating waves in the film at the depth z. Assuming hemiellipsoidal nanoparticles tilted from the surface normal by a tilt angle of χ about the x axis, one has

$$F(\vec{q}) = \frac{\pi}{2}\int_0^{D_z} \exp(-iQ_z z)\, D_x D_y G_z \frac{J_1(g)}{g} dz, \quad (10)$$

with

$$\vec{Q} = \begin{pmatrix} 1 & 0 & 0 \\ 0 & \cos(\chi) & \sin(\chi) \\ 0 & -\sin(\chi) & \cos(\chi) \end{pmatrix} \vec{q}, \quad (11)$$

$G_z = \sqrt{1-(z/D_z)^2}$ and $g = G_z\sqrt{(Q_x^2 D_x^2 + Q_y^2 D_y^2)/4}$.

Besides, taking into account correlated roughness effects, replication of topography from the Ag nanoparticles to the surface of the Al_2O_3 capping layer implies that the form factor is the sum of three terms:[58,59]

$$|\mathcal{F}(\vec{q})|^2 = |\mathcal{F}_{Ag}(\vec{q})|^2 + |\mathcal{F}_{Al_2O_3}(\vec{q})|^2 + 2|\mathcal{F}_{Ag}(\vec{q})||\mathcal{F}_{Al_2O_3}(\vec{q})|\cos(\vec{q}\cdot\vec{r}), \quad (12)$$

where $\mathcal{F}_{Ag}$ is the form factor of the buried Ag nanoparticles [Eq. (9)], $\mathcal{F}_{Al_2O_3}$ is the form factor of the surface corrugations [Eq. (4)], and the third term describes the interference between them ($\vec{r}$ defines the coordinates of the surface corrugations with respect to the Ag nanoparticles).

Figure 9 exhibits out-of-plane ($2\theta_f$,α_f) maps calculated at $\varphi = 0°$ using Eqs. (8)–(12) for Ag nanoparticle patterns sandwiched between 20-nm-thick Al_2O_3 layers deposited on a Si substrate ($\lambda = 0.16$ nm and $\alpha_i = 0.3°$). The Ag nanoparticles were considered as hemispheroids with in-plane diameter $D_x = D_y = 8$ nm and height $D_z = 4$ nm. The structure factor was computed by assuming a square lattice with $\Lambda_x = \Lambda_y = 20$ nm and $\xi_x = \xi_y = 250$ nm. The GISAXS intensity calculated when assuming nanoparticles grown on a flat Al_2O_3 buffer layer (i.e., $\chi = 0°$) and covered by a flat Al_2O_3 capping layer [i.e., only the first term is taken into account in Eq. (12)] displays symmetric streaks [Fig. 9(a)], which are smoothly modulated along the vertical direction as seen in line profiles presented in Fig. 10. Such damped fringes arise from interferences between the upward and

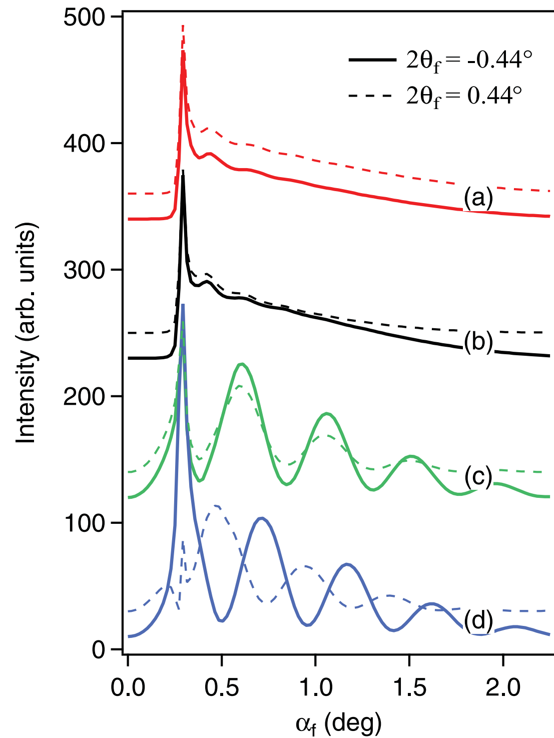

FIG. 10. (Color online) Line profiles drawn at $2\theta_f = -0.44°$ and $2\theta_f = 0.44°$ corresponding to the simulated GISAXS patterns shown in Figs. 9(a)–9(d). Curves are shifted upward for clarity.

downward propagating waves into the stratified film and, accordingly, their period depends on the thicknesses of both the buffer and capping layers.[59,60] Tilting the nanoparticles by an angle $\chi = 21.8^\circ$, corresponding to the positive slope γ_+ of a fictitious rippled interface (with a symmetric sawtooth profile), leads to similar results although the GISAXS signal presents a slight asymmetry with $AR < 0$ [Fig. 9(b)]. In contrast, as a result of the cross term in Eq. (12), correlated roughness effects give rise to strong vertical modulations whose periodicity is inversely proportional to the thickness of the Al_2O_3 capping layer t_{cap} and is independent of the thickness of the buffer layer [Figs. 9(c), 9(d), and 10]. GISAXS simulations presented in Figs. 9(c) and 9(d) were performed by supposing the presence of hemispheroidal nanodots on the surface of the Al_2O_3 capping layer with diameter $D_{dot} = D_y$ and height $H_{dot} = D_z$. Assuming the nanodots to be located above the Ag nanoparticles [i.e., in Eq. (12), $\vec{q} \cdot \vec{r} = q_x\delta_x + q_y\delta_y + q_z\delta_z$ with $\delta_x = \delta_y = 0$ and $\delta_z = t_{cap}$] results in the appearance of horizontal fringes in the $(2\theta_f,\alpha_f)$ map shown in Fig. 9(c), so that the vertical line profiles drawn at $2\theta_f = -0.44^\circ$ and $2\theta_f = 0.44^\circ$ oscillate in phase (Fig. 10). However, when considering the nanodots placed above the buried ripples ($\delta_y = \Lambda_y/4$), inclined fringes are obtained in the corresponding $(2\theta_f,\alpha_f)$ map [Fig. 9(d)], leading to a phase shift between the vertical line profiles drawn at $2\theta_f = -0.44^\circ$ and $2\theta_f = 0.44^\circ$ (Fig. 10).

C. Results

Figures 11(a) and 12(a) show the experimental $(2\theta_f,\alpha_f)$ maps taken at $\varphi = 0^\circ$ for the Al_2O_3-capped Ag nanoparticles grown on rippled Al_2O_3 thin films with Ag amounts of 1.4 and 2.8 nm, respectively. In both cases, the 2D GISAXS patterns exhibit sharp vertical streaks at $2\theta_f \approx \pm 0.42^\circ$, which are very obviously modulated with a phase shift in agreement with the simulations presented in Fig. 9(d) assuming roughness correlations with $\chi = \gamma_+$ and $\delta_y = \Lambda_y/4$. Qualitatively, these results confirm our HAADF-STEM observations showing replication of the lateral order between ripples by the nanoparticles as well as replication of the topography of the buried rippled interface by the surface roughness of the Al_2O_3 capping layer (Fig. 8). In contrast, the 2D GISAXS patterns displayed in Figs. 11(b) and 12(b), which were obtained with the x-ray beam perpendicular to the ripples ($\varphi = 90^\circ$), show two broad lobes located at $2\theta_f \approx \pm 0.81^\circ$ and $2\theta_f \approx \pm 0.52^\circ$, respectively. These scattering signals are typical of a 2D distribution of nanoparticles with only short-range order in a direction parallel to the ripples. In that case, the GISAXS intensity is also modulated in the vertical direction, but more slightly and without phase shift, thus indicating weak roughness correlations with $\delta_x = 0$. A schematic representation of the corresponding capping-layer surface is depicted in Fig. 11(e), which shows the replication direction in a real-space picture.

For a quantitative analysis, 2D GISAXS patterns taken at $\varphi = 90^\circ$ were first fitted assuming monodisperse hemiellipsoidal Ag nanoparticles and surface nanodots with $D_{xdot} = D_x = 1.2D_y$, $H_{xdot} = \kappa_{zx}D_z$, and $\chi = \gamma_+$ (γ_+ was fixed from the GISAXS analysis of as-etched Al_2O_3 thin films, as described in Sec. II C2). In addition to D_x, D_z, and κ_{zx}, 2D data fitting allowed to determine the interparticle distance Λ_x along the x direction as well as the corresponding correlation length ξ_x and the vertical distance between the Ag nanoparticles and the surface nanodots δ_{zx}. Then, 2D GISAXS patterns taken at $\varphi = 0^\circ$ were fitted to retrieve the interparticle distance Λ_y along the y direction, and the corresponding correlation length ξ_y and vertical particle-dot distance δ_{zy}, while the dot height was considered as $H_{ydot} = \kappa_{zy}D_z$ and the lateral particle-dot distance $\delta_y = \Lambda_y/4$ was fixed according to the cross-sectional HAADF-STEM observations and previous GISAXS simulations. The best-fit parameters are reported in Table II and the corresponding simulated maps are presented in Figs. 11(c) and 11(d) and Figs. 12(c) and 12(d).

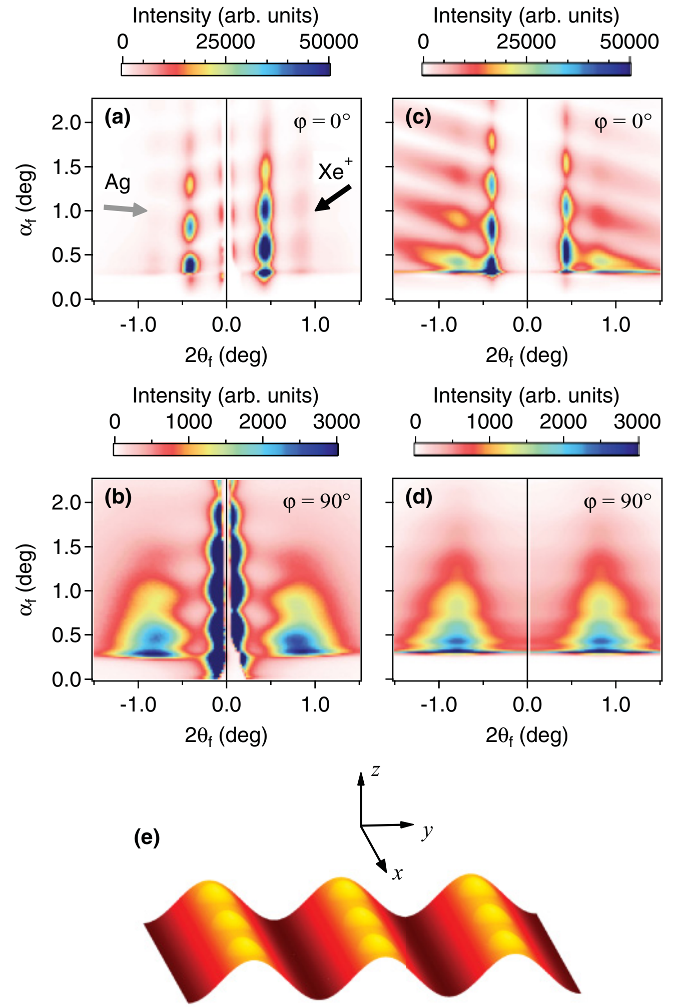

FIG. 11. (Color online) GISAXS analysis of Al_2O_3-capped Ag nanoparticles grown on a rippled Al_2O_3 thin film (Ag amount of 1.4 nm). Experimental out-of-plane $(2\theta_f,\alpha_f)$ maps at (a) $\varphi = 0^\circ$ (x-ray beam parallel to the x direction) and (b) $\varphi = 90^\circ$ (x-ray beam parallel to the y direction). The directions of the Xe^+ ion beam and Ag atomic flux are indicated by the black and gray arrows in (a). (c), (d) Simulated out-of-plane maps. (e) Schematic picture of the capping-layer surface corresponding to the configuration described in Fig. 9(d).

Overall, the matching between the experimental and simulated data is fairly good both at $\varphi = 0^\circ$ and $\varphi = 90^\circ$, especially in terms of position and intensity of the maxima aligned along the first order scattering streaks and lobes. However, the simulations at $\varphi = 0^\circ$ yield second order scattering streaks

TABLE II. Parameters retrieved from the GISAXS analysis of Al_2O_3-capped Ag nanoparticles grown on rippled Al_2O_3 thin films. Assuming hemiellipsoidal Ag nanoparticles and surface nanodots with roughness correlations, D_i, Λ_i, ξ_i, and δ_{zi} are the size, interparticle distance, correlation length, and vertical particle-dot distance along direction i. The dot height is $H_{i\text{dot}} = \kappa_{zi} D_z$. For the experimental data fitting, $D_y = D_x/1.2$, $\delta_x = 0$, $\delta_y = \Lambda_y/4$, and $\chi = \gamma_+$ were fixed.

Ag amount (nm)	D_z (nm)	D_x (nm)	Λ_x (nm)	ξ_x (nm)	δ_{zx} (nm)	κ_{zx}	Λ_y (nm)	ξ_y (nm)	δ_{zy} (nm)	κ_{zy}
1.4	3.5	5.4	9.0	24.5	22.2	0.04	21.7	276	18.4	0.32
2.8	5.2	7.3	12.5	24.7	22.2	0.39	21.6	266	18.0	0.93

together with inclined lines of diffuse scattering that are not present experimentally. These discrepancies can be due to the various approximations made in the model, e.g., the size and shape distributions as well as the particle-particle and particle-dot positional fluctuations are not included here for the sake of simplicity. In Table II, our results show that the in-plane (D_x) and out-of-plane (D_z) sizes of the Ag nanoparticles increase with the deposited Ag amount, as expected. This nanoparticle coarsening is associated with an increase of the interparticle distance along the x direction (Λ_x) whereas the interparticle distance along the y direction (Λ_y) remains constant close to the ripple period as determined from the GISAXS analysis of the as-etched Al_2O_3 thin film (Table I). Moreover, it can be seen that the normalized correlation length is much greater in the y direction ($\xi_y/\Lambda_y \sim 12$) than in the x direction ($\xi_x/\Lambda_x \sim 2$), which confirm that the degree of ordering between nanoparticles is higher in the direction perpendicular to the ripples. For comparison, AFM images [Fig. 13(a)] and corresponding 2D and 1D power spectral densities (PSDs) show how ordered the surface nanodots are [Fig. 13(b)]. Since the PSD is supposed to be directly proportional to the scattered intensity arising from the surface corrugations [second term in Eq. (12)], the 1D PSD along the y direction exhibits a narrow first peak at $k_y \approx 0.045$ nm^{-1} (i.e., $\Lambda_y \approx 22.2$ nm corresponding to the ripple period) together

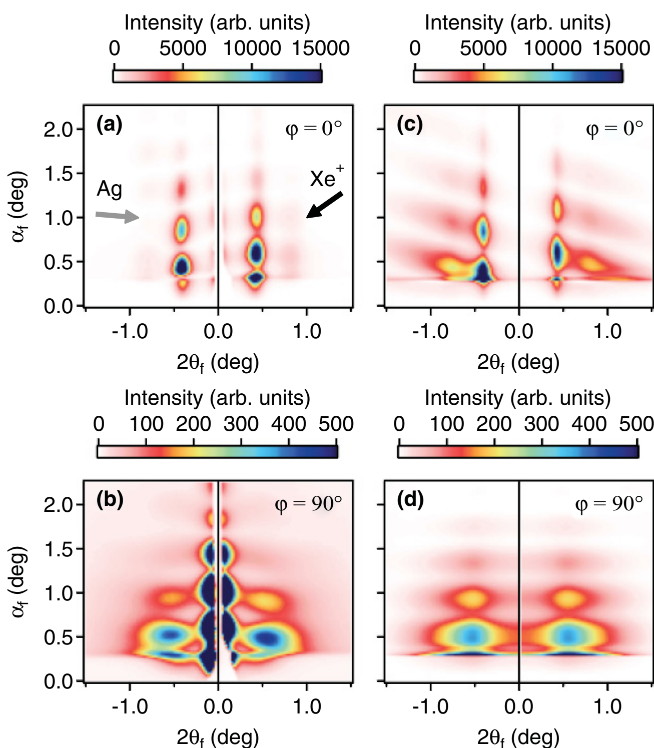

FIG. 12. (Color online) GISAXS analysis of Al_2O_3-capped Ag nanoparticles grown on a rippled Al_2O_3 thin film (Ag amount of 2.8 nm). Experimental out-of-plane ($2\theta_f$,α_f) maps at (a) $\varphi = 0^\circ$ and (b) $\varphi = 90^\circ$. The directions of the Xe^+ ion beam and Ag atomic flux are indicated by the black and gray arrows in (a). (c), (d) Simulated out-of-plane maps.

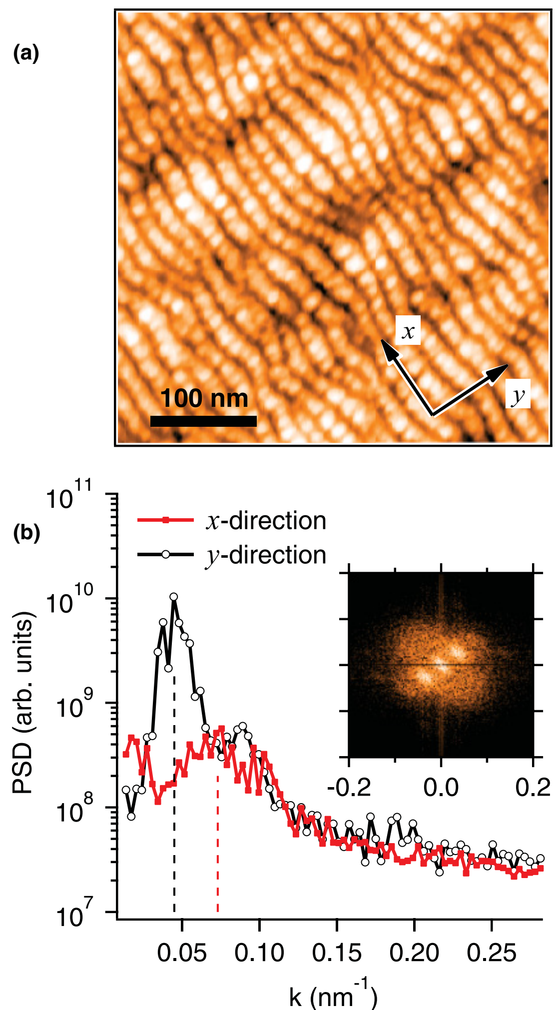

FIG. 13. (Color online) (a) AFM image of the surface morphology obtained with Al_2O_3-capped Ag nanoparticles grown on a rippled Al_2O_3 thin film (Ag amount of 1.4 nm). (b) Corresponding 2D (inset) and 1D power spectral densities (PSD).

with higher order peaks, in agreement with the GISAXS results. Furthermore, a single broad peak is revealed in the x direction at a higher spatial frequency $k_y \approx 0.073$ nm^{-1}, corresponding to an interdot distance $\Lambda_x \approx 13.7$ nm slightly higher than the interparticle distance determined by GISAXS. This deviation suggests that the smallest particles of the buried assembly do not give rise to a replication detectable by AFM, resulting in a smaller apparent areal density of surface dots.[59]

Finally, the quantitative analysis of our GISAXS data show that the vertical particle-dot distance (δ_{zx} and δ_{zy}) is close to the thickness of the Al_2O_3 capping layer ($t_{cap} \sim$ 20 nm) and that the degree of roughness correlation (κ_{zx} and κ_{zy}) increases with the deposited Ag amount, i.e., the height of the Ag nanoparticles. These results indicate that, while the capping layer undergoes a conformal growth with respect to the prepatterned buffer layer, the amplitude of the surface modulation is further increased by the presence of the nanoparticles as confirmed by AFM observations in Fig. 13(a). However, the degree of roughness correlation appears much higher in the y direction ($\kappa_{zy} > \kappa_{zx}$), while the corresponding vertical particle-dot distance is smaller ($\delta_{zy} < \delta_{zx}$), whatever the deposited Ag amount. Accordingly, the roughness profile of the Al_2O_3 surface appears smoother in the x direction ($\parallel$ ripples) than in the y direction ($\perp$ ripples). It is worth noting that, by taking advantage of the periodic repetition of this phenomenon, the formation of 3D arrays of nanoparticles with very narrow size distribution and regularly ordered within a single large domain can be achieved by (amorphous) multilayer deposition.[24]

IV. CONCLUSION

In summary, we reported on the measurement and quantitative analysis of 3D GISAXS maps originating from nanoripple and nanoparticle patterns prepared by IBS. The combined use of a 2D detector and azimuthal in-plane scans of the sample enabled us to obtain accurate morphological characteristics and to determine unambiguously, e.g., the shape asymmetry and the length of the ripples. Despite extensive theoretical and experimental works, the mechanisms of ripple formation by IBS are still not completely understood and require further research efforts. In this respect, the approach described here associated with *in situ* monitoring and high brilliance synchrotron radiation may be very useful. Our results also show that the lateral order of the nanoripple patterns can be transferred to arrays of nanoparticles by subsequent IBS deposition at glancing incidence. GISAXS experiments clearly demonstrate that the rippled surfaces are selectively decorated by the nanoparticles on the facets that face the incoming atomic flux. In addition, under normal incidence deposition, the growth of an additional capping layer proceeds conformal with respect to the modulation of the prepatterned buffer layer. Since the size and spacing (in-plane and out-of-plane) of the nanoparticles can be controlled independently and directly by varying the thickness of the layers and the ripple period, tunable 3D ordering can be induced in subsequently deposited discontinuous multilayers. Such an approach might offer considerable possibilities to tailor electrical, optical, or magnetic properties of functional thin films or nanostructures.

ACKNOWLEDGMENTS

This work has been carried out within the QMAX project No. ANR-09-NANO-031 funded by the French National Agency (ANR) in the frame of its 2009 programme in Nanosciences, Nanotechnologies and Nanosystems (P3N2009). We acknowledge the assistance of the ESRF and ID01 staff for beam availability during the GISAXS experiments. We also thank P. Guérin for his invaluable help during the sample preparation and L. Simonot for AFM characterizations.

*david.babonneau@univ-poitiers.fr

[1] J. Muñoz-García, L. Vásquez, R. Cuerno, J. A. Sánchez-García, M. Castro, and R. Gago, in *Towards Functional Nanomaterials*, edited by Z. M. Wang (Springer, New York, 2009), pp. 323–398.

[2] W. L. Chan and E. Chason, J. Appl. Phys. **101**, 121301 (2007).

[3] U. Valbusa, C. Boragno, and F. Buatier de Mongeot, J. Phys.: Condens. Matter **14**, 8153 (2002).

[4] M. A. Makeev, R. Cuerno, and A.-L. Barabási, Nucl. Instrum. Methods Phys. Res., Sect. B **197**, 185 (2002).

[5] C. Boragno and R. Felici, J. Phys.: Condens. Matter **21**, 224006 (2009).

[6] D. Carbone, A. Biermanns, B. Ziberi, F. Frost, O. Plantevin, U. Pietsch, and T. H. Metzger, J. Phys.: Condens. Matter **21**, 224007 (2009).

[7] R. L. Headrick and H. Zhou, J. Phys.: Condens. Matter **21**, 224005 (2009).

[8] Q. Wei, J. Lian, S. Zhu, W. Li, K. Sun, and L. Wang, Chem. Phys. Lett. **452**, 124 (2008).

[9] R. M. Bradley and J. M. E. Harper, J. Vac. Sci. Technol. A **6**, 2390 (1988).

[10] R. Cuerno and A.-L. Barabási, Phys. Rev. Lett. **74**, 4746 (1995).

[11] M. A. Makeev and A.-L. Barabási, Appl. Phys. Lett. **71**, 2800 (1997).

[12] S. Facsko, T. Bobek, A. Stahl, H. Kurz, and T. Dekorsy, Phys. Rev. B **69**, 153412 (2004).

[13] J. Muñoz-García, M. Castro, and R. Cuerno, Phys. Rev. Lett. **96**, 086101 (2006).

[14] H. Zhou, Y. Wang, L. Zhou, R. L. Headrick, A. S. Özcan, Y. Wang, G. Özaydin, K. F. Ludwig Jr., and D. P. Siddins, Phys. Rev. B **75**, 155416 (2007).

[15] G. Carter, J. Appl. Phys. **85**, 455 (1999).

[16] P. Sigmund, Phys. Rev. **184**, 383 (1969).

[17] C. C. Umbach, R. L. Headrick, and K.-C. Chang, Phys. Rev. Lett. **87**, 246104 (2001).

[18] A. Keller, S. Facsko, and W. Möller, J. Phys.: Condens. Matter **21**, 495305 (2009).

[19] A. Molle, F. Buatier de Mongeot, C. Boragno, R. Moroni, F. Granone, D. Sekiba, R. Buzio, U. Valbusa, R. Felici, and C. Quiros, Appl. Phys. Lett. **86**, 141906 (2005).

[20]T. W. H. Oates, A. Keller, S. Noda, and S. Facsko, Appl. Phys. Lett. **93**, 063106 (2008).
[21]S. Numazawa, M. Ranjan, K.-H. Heinig, S. Facsko, and R. Smith, J. Phys.: Condens. Matter **23**, 222203 (2011).
[22]A. Keller, L. Peverini, J. Grenzer, G. J. Kovacs, A. Mücklich, and S. Facsko, Phys. Rev. B **84**, 035423 (2011).
[23]J. Petersen and S. G. Mayr, J. Appl. Phys. **103**, 023520 (2008).
[24]M. Buljan, J. Grenzer, A. Keller, N. Radić, V. Valeš, S. Bernstorff, T. Cornelius, H. T. Metzger, and V. Holý, Phys. Rev. B **82**, 125316 (2010).
[25]R. Moroni, D. Sekiba, F. Buatier de Mongeot, G. Gonella, C. Boragno, L. Mattera, and U. Valbusa, Phys. Rev. Lett. **91**, 167207 (2003).
[26]F. Bisio, R. Moroni, F. Buatier de Mongeot, M. Canepa, and L. Mattera, Phys. Rev. Lett. **96**, 057204 (2006).
[27]M. O. Liedke, B. Liedke, A. Keller, B. Hillebrands, A. Mücklich, S. Facsko, and J. Fassbender, Phys. Rev. B **75**, 220407 (2007).
[28]J. Fassbender, T. Strache, M. O. Liedke, D. Markó, S. Wintz, K. Lenz, A. Keller, S. Facsko, I. Mönch, and J. McCord, New J. Phys. **11**, 125002 (2009).
[29]M. Körner, K. Lenz, M. O. Liedke, T. Strache, A. Mücklich, A. Keller, S. Facsko, and J. Fassbender, Phys. Rev. B **80**, 214401 (2009).
[30]K. V. Sarathlal, D. Kumar, and A. Gupta, Appl. Phys. Lett. **98**, 123111 (2011).
[31]K. V. Sarathlal, D. Kumar, V. Ganesan, and A. Gupta, Appl. Surf. Sci. **258**, 4116 (2012).
[32]A. Toma, D. Chiappe, D. Massabo, C. Boragno, and F. Buatier de Mongeot, Appl. Phys. Lett. **93**, 163104 (2008).
[33]T. W. H. Oates, A. Keller, S. Facsko, and A. Mücklich, Plasmonics **2**, 47 (2007).
[34]M. Ranjan, T. W. H. Oates, S. Facsko, and W. Möller, Opt. Lett. **35**, 2576 (2010).
[35]S. Camelio, D. Babonneau, D. Lantiat, L. Simonot, and F. Pailloux, Phys. Rev. B **80**, 155434 (2009).
[36]D. Babonneau, S. Camelio, L. Simonot, F. Pailloux, P. Guérin, B. Lamongie, and O. Lyon, Europhys. Lett. **93**, 26005 (2011).
[37]M. V. Ramana Murty, T. Curcic, A. Judy, B. H. Cooper, A. R. Woll, J. D. Brock, S. Kycia, and R. L. Headrick, Phys. Rev. Lett. **80**, 4713 (1998).
[38]O. Malis, J. D. Brock, R. L. Headrick, M.-S. Yi, and J. M. Pomeroy, Phys. Rev. B **66**, 035408 (2002).
[39]C. Boragno, F. Buatier de Mongeot, G. Costantini, U. Valbusa, R. Felici, D.-M. Smilgies, and S. Ferrer, Phys. Rev. B **65**, 153406 (2002).
[40]T. C. Kim, M. H. Jo, Y. Kim, D. Y. Noh, B. Kahng, and J.-S. Kim, Phys. Rev. B **73**, 125425 (2006).
[41]F. Ludwig Jr., C. R. Eddy Jr., O. Malis, and R. L. Headrick, Appl. Phys. Lett. **81**, 2770 (2002).
[42]G. Ozaydin, K. F. Ludwig Jr., H. Zhou, and R. L. Headrick, J. Vac. Sci. Technol. B **26**, 551 (2008).
[43]S. Hazra, T. K. Chini, M. K. Sanyal, J. Grenzer, and U. Pietsch, Phys. Rev. B **70**, 121307 (2004).
[44]R. Gago, L. Vázquez, O. Plantevin, J. A. Sánchez-García, M. Varela, M. C. Ballesteros, J. M. Albella, and T. H. Metzger, Phys. Rev. B **73**, 155414 (2006).
[45]R. Gago, L. Vázquez, O. Plantevin, T. H. Metzger, J. Muñoz-García, R. Cuerno, and M. Castro, Appl. Phys. Lett. **89**, 233101 (2006).
[46]O. Plantevin, R. Gago, L. Vázquez, A. Biermanns, and T. H. Metzger, Appl. Phys. Lett. **91**, 113105 (2007).
[47]A. Biermanns, U. Pietsch, J. Grenzer, A. Hanisch, S. Facsko, G. Carbone, and T. H. Metzger, J. Appl. Phys. **104**, 044312 (2008).
[48]D. Carbone, A. Alija, O. Plantevin, R. Gago, S. Facsko, and T. H. Metzger, Nanotechnology **19**, 035304 (2008).
[49]D. Babonneau, A. Naudon, T. Cabioc'h, and O. Lyon, J. Appl. Crystallogr. **33**, 437 (2000).
[50]J. S. Pedersen, J. Appl. Crystallogr. **27**, 595 (1994).
[51]M. Rauscher, R. Paniago, H. Metzger, Z. Kovats, J. Domke, J. Peisl, H.-D. Pfannes, J. Schulze, and I. Eisele, J. Appl. Phys. **86**, 6763 (1999).
[52]F. Abélès, Ann. Phys. (Paris) **5**, 596 (1950).
[53]A. Gibaud, in *X-ray and Neutron Reflectivity: Principles and Applications*, edited by A. Gibaud and J. Daillant (Springer, Paris, 1999), pp. 87–115.
[54]F. Leroy, R. Lazzari, and G. Renaud, Acta Crystallogr. Sect. A **60**, 565 (2004).
[55]D. Babonneau, J. Appl. Crystallogr. **43**, 929 (2010).
[56]B. Ziberi, F. Frost, T. Höche, and B. Rauschenbach, Phys. Rev. B **72**, 235310 (2005).
[57]W. H. Press, B. P. Flannery, S. A. Teukolski, and W. T. Vetterling, *Numerical Recipes in C* (Cambridge University Press, New York, 1992).
[58]F. Leroy, G. Renaud, A. Letoublon, R. Lazzari, C. Mottet, and J. Goniakowski, Phys. Rev. Lett. **95**, 185501 (2005).
[59]D. Babonneau, S. Camelio, D. Lantiat, L. Simonot, and A. Michel, Phys. Rev. B **80**, 155446 (2009).
[60]Z. Jiang, D. R. Lee, S. Narayanan, J. Wang, and S. K. Sinha, Phys. Rev. B **84**, 075440 (2011).